Modeling and analysis of harmonic resonance in a power electronics based AC power system

Wang, Xiongfei; Blaabjerg, Frede; Chen, Zhe; Wu, Weimin

Published in:
Proceedings of the 2013 IEEE Energy Conversion Congress and Exposition (ECCE)

DOI (link to publication from Publisher):
10.1109/ECCE.2013.6647408

Publication date:
2013

Document Version
Early version, also known as pre-print

Digital Object Identifier (DOI): 10.1109/ECCE.2013.6647408

IEEE Energy Conversion Congress and Exposition (ECCE), pp. 5229-5236, Sept. 2013.

Modeling and Analysis of Harmonic Resonance in a Power Electronics Based AC Power System

Xiongfei Wang
Frede Blaabjerg
Zhe Chen
Weimin Wu

Suggested Citation

X. Wang, F. Blaabjerg, Z. Chen, and W. Wu, "Modeling and analysis of harmonic resonance in a power electronics based AC power system," in *Proc. IEEE ECCE* 2013, pp. 5229-5236.

Modeling and Analysis of Harmonic Resonance in a Power Electronics Based AC Power System

Xiongfei Wang, Frede Blaabjerg, Zhe Chen
Department of Energy Technology
Aalborg University, Aalborg, Denmark
xwa@et.aau.dk, fbl@et.aau.dk, zch@et.aau.dk

Weimin Wu
Department of Electrical Engineering
Shanghai Maritime University, Shanghai, China
wwu@et.aau.dk

***Abstract*—The dynamic interactions among the interconnected power converters may bring in harmonic resonance in a power electronics based power system. This paper addresses this issue in a power system dominated by multiple current- and voltage-controlled inverters with *LCL*- and *LC*-filters. The impedance-based analysis approach is adopted and expanded to a meshed and balanced three-phase power network. An impedance ratio derivation method is proposed based on the nodal admittance matrix. By this means, the contribution of each inverter to the system resonance modes can be easily predicted by the Nyquist stability criterion. To validate the theoretical analysis, the time domain simulations and experimental tests on a three-inverter-based system are presented.**

I. INTRODUCTION

The proportion of power electronics apparatus in electric power systems keeps growing in recent years, driven by the rapid development of renewable power sources and energy-efficient drives [1]. As a consequence, the power electronics based power systems are becoming important components of the power grids, such as wind farms [2], photovoltaic power plants [3], microgrids [4], and electric rail systems [5]. These systems provide superior features to build the modern power grids, such as the full controllability, sustainability, and high efficiency, but bring also new challenges [6]. The small time constants of switching power converters considerably reduce the system damping. The dynamic interactions between the power electronics based power sources and loads may bring in a wide frequency range of harmonic resonances [7]. This problem is further aggravated by the shunt capacitors, which can be found in the widely used *LCL*- or *LC*-filters of power converters and in the underground cables [8]. The resonance propagation triggered by the shunt capacitors is becoming an important power quality problem [9].

The continuous research efforts have been made to deal with the harmonic resonance in the power electronics based power systems. A general analysis approach is to build the state-space model for the power system, and then identify the resonance modes based on the eigenvalues and eigenvectors of the system state matrix [10]. This method has been mostly used for the traditional power systems with a large number of machines [11], where the effect of the individual components or subsystems on the system stability is usually hidden in the state matrix. In [12], the Component Connection Method (CCM) that takes advantage of matrix algebra and sparsity is introduced for the stability analysis of the High-Voltage DC (HVDC) systems. Unlike the general state-space models, the CCM decomposes the power system into several subsystems by components, and depicts the system dynamic behavior by assembling the linearized models of subsystems. Hence, it is more intuitive than the state-space analysis for predicting the impacts of subsystems on the global system stability. Later on, the CCM is expanded into the multivariable frequency domain [13], where the system resonances are evaluated by the generalized Nyquist stability criterion [14].

The impedance-based approach, originally introduced for designing the input filters of the DC-DC converters [15], has provided another way to analyze the resonances. Similarly to the CCM, the impedance-based approach is also based on the linearized models of converters [16]. However, instead of synthesizing the system transfer matrices as in the CCM, the impedance-based approach predicts the harmonic resonance by the ratio between the output impedance of each converter and the equivalent system impedance derived at the Point of Connection (PoC) of each converter. Thus, a more insightful and design-oriented resonance analysis can be achieved [17]. Several applications of the impedance-based approach can be found in the power electronics based AC power systems, e.g. the cascaded sour-load inverter system [18], the parallel grid-connected converters with *LCL*-filters [19], and the parallel uninterruptible power supply inverters with *LC*-filters [20]. However, in all these cases, the effect of connection network structures is often overlooked. Few of them have considered the operations with multiple voltage- and current-controlled inverters.

This paper attempts to fill in this gap by expanding the impedance-based resonance analysis to a three phase meshed and balanced power system, where a voltage-controlled and two current-controlled inverters with *LC*- and *LCL*-filters are interconnected. The harmonic resonances that result from the interactions among these inverters as well as other passive

This work was supported by European Research Council (ERC) Advanced Grant – "Harmonic identification, mitigation and control in power electronics based power systems (HARMONY)".

system components are evaluated. By the help of the nodal admittance matrix, an impedance ratio derivation method is proposed in order to predict how each inverter contributes to the system resonances. Lastly, the time domain simulations and experimental results are presented to further validate the theoretical analysis in the frequency domain.

II. System Modeling and Analysis Technique

This section reviews the CCM and the impedance-based approach for modeling and analysis of harmonic resonance in the power electronics based AC power system.

A. System Description

Fig. 1 shows a simplified one-line diagram for a three-phase balanced power system which is considered in this work, where a voltage-controlled and two current-controlled inverters are interconnected as a meshed network via power cables. The voltage-controlled inverter regulates the system frequency and voltage amplitude, and the current-controlled inverters operate with unity power factor.

In the system, the shunt capacitors in the *LC*- and *LCL*-filters of the inverters and the power cables may bring in the harmonic resonance with the cable inductances. Further, the output impedance of an inverter may exhibit a non-positive real part in a certain frequency range, which depends on its control loop dynamic [21]. Consequently, the non-intentional harmonic resonance may be triggered due to the interactions among the controllers of the inverters [22]. This necessitates the use of a design-oriented analysis method to predict how the inverters interact with each other and affect the harmonic resonance in the system.

B. CCM

Fig. 2 depicts the block diagram of the CCM used for the studied system. The current- and voltage-controlled inverters are modeled by the Norton and Thevenin equivalent circuits, respectively, at their PoC, while the meshed network can be modeled by the nodal admittance or impedance matrix. Thus, the system transfer matrices can be derived as

$$y(s) = \mathbf{G_{cl}}(s)u(s) - \mathbf{G_{cd}}(s)d(s) \tag{1}$$

$$y(s) = \left[\mathbf{I} + \mathbf{G_{nw}}(s)\mathbf{G_{cd}}(s)\right]^{-1}\mathbf{G_{cl}}(s)u(s) \tag{2}$$

where $\mathbf{G_{nw}}(s)$ is the network transfer function, and

$$y(s) = [V_1(s), i_{g2}(s), i_{g3}(s)]^{\mathrm{T}}$$
$$u(s) = [V_1^*(s), i_{g2}^*(s), i_{g3}^*(s)]^{\mathrm{T}}$$
$$\mathbf{G_{cl}}(s) = \mathrm{diag}[G_{clv,1}(s), G_{cli,2}(s), G_{cli,3}(s)]$$
$$\mathbf{G_{cd}}(s) = \mathrm{diag}[Z_{ov,1}(s), Y_{oi,2}(s), Y_{oi,3}(s)]$$

where $G_{clv,1}(s)$, $G_{cli,2}(s)$, and $G_{cli,3}(s)$ denote the voltage and current reference-to-output transfer functions of the voltage- and current-controlled inverters, respectively. $Z_{ov,1}(s)$, $Y_{oi,2}(s)$, and $Y_{oi,3}(s)$ are the output impedance and admittances of the voltage- and current-controlled inverters, respectively. Thus,

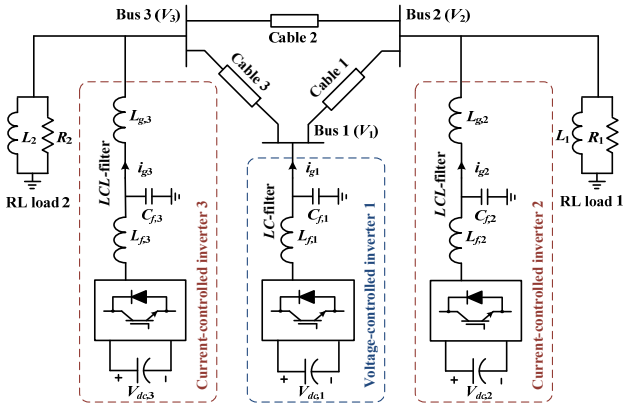

Fig. 1. Simplified one-line diagram of a power electronics based AC power system.

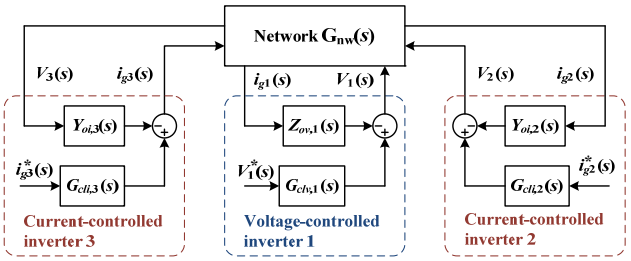

Fig. 2. Block diagram of the CCM used for the studied power system.

the system resonance can be predicted by the loop transfer matrix $[\mathbf{I} + \mathbf{G_{nw}}(s)\mathbf{G_{cd}}(s)]^{-1}$ provided that the closed-loop response of each inverter $\mathbf{G_{cl}}(s)$ is stable.

It is obvious that the CCM decomposes the power system into three decentralized feedback loops by the inverters. The effect of the inverter controllers and the associated physical components on the system resonances can be modeled. Also, the decentralized stabilizing control loops can be developed based on this modeling method [23].

C. Impedance-Based Approach

Fig. 3 depicts the impedance-based equivalent circuits for the voltage- and current-controlled inverters. It is interesting to note that the terminal behavioral models of the inverters are also required in this approach [16]. However, different from the CCM, the interactions between one inverter and the others are modeled by the equivalent impedance/admittance for the rest of the system, i.e. $Z_{lv}(s)$ or $Y_{li,m}(s)$ ($m = 2, 3$).

The closed-loop transfer functions of the inverters can be derived as follows

$$\frac{V_1(s)}{G_{clv,1}(s)V_1^*(s)} = \frac{1}{1 + \dfrac{Z_{ov,1}(s)}{Z_{lv,1}(s)}} \tag{3}$$

$$\frac{i_{gm}(s)}{G_{cli,m}(s)i_{gm}^*(s)} = \frac{1}{1 + \dfrac{Y_{oi,m}(s)}{Y_{li,m}(s)}} \tag{4}$$

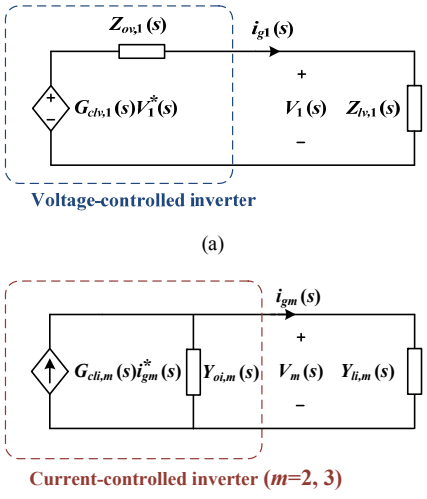

Fig. 3. Impedance-based equivalent models for (a) the voltage- and (b) the current-controlled inverters.

Hence, if the terminal behavior of the inverters at their PoC, i.e. $G_{clv,1}(s)$ and $G_{cli,m}(s)$ are designed stable, the stability of the voltage and current at each system bus can be determined by the following impedance ratios

$$T_{mv}(s)=\frac{Z_{ov,1}(s)}{Z_{lv,1}(s)},\quad T_{mc}(s)=\frac{Y_{oi,m}(s)}{Y_{li,m}(s)} \tag{5}$$

which are also termed as the minor feedback loop gains [17]. The design specifications for the inverters output impedances can thus be derived to preserve the power system stability.

III. Modeling of Inverters

To perform the harmonic resonance analysis by using the impedance-based approach, the impedance-based equivalent models of inverters are derived in this section. Also, the constant DC-link voltages of the inverters are assumed, since the bandwidth of the DC-link voltage control are designed lower than the system fundamental frequency.

A. Voltage-Controlled Inverters

Fig. 4 illustrates the control block diagram of the voltage-controlled inverter. The control system is implemented in the stationary frame, including the inner Proportional (P) current controller and the outer Proportional Resonant (PR) voltage controller. The three-phase inverters without neutral wire can be transformed into two independent single-phase systems in the $\alpha\beta$-frame. Thus, the inverter dynamics can be modeled as a real scalar system. Also, due to the assumed constant DC-link voltage, the inverter can be modeled by the *LC*-filter.

From Fig. 4, the reference-to-output transfer function and the closed-loop output impedance can be given by

$$G_{clv,1}(s)=\frac{T_v(s)}{1+T_v(s)},\quad Z_{ov,1}(s)=\frac{Z_{oi}(s)}{1+T_v(s)} \tag{6}$$

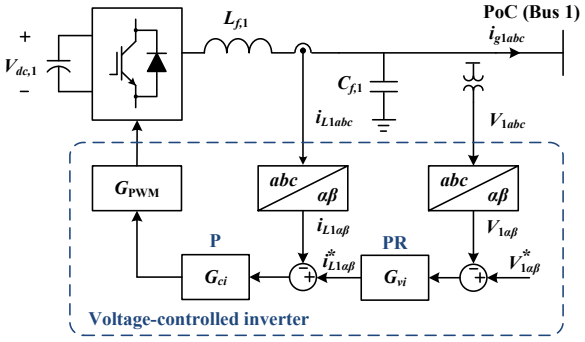

Fig. 4. Control block diagram of the voltage-controlled inverter.

where $T_v(s)$ is the open-loop gain of the voltage control loop, and $Z_{oi}(s)$ is the open-loop output impedance evaluated with the outer voltage loop open and the inner current loop closed, which are expressed as [24]

$$T_v(s)=\frac{G_{vi}(s)G_{ci}(s)G_{PWM}(s)Z_{Cf,1}(s)}{Z_{Lf,1}(s)+Z_{Cf,1}(s)+G_{ci}(s)G_{PWM}(s)} \tag{7}$$

$$Z_{oi}(s)=\frac{Z_{Cf,1}(s)\left[Z_{Lf,1}(s)+G_{ci}(s)G_{PWM}(s)\right]}{Z_{Lf,1}(s)+Z_{Cf,1}(s)+G_{ci}(s)G_{PWM}(s)} \tag{8}$$

where $Z_{Lf,1}(s)$ and $Z_{Cf,1}(s)$ are the impedances of the filter inductor and capacitor, respectively. $G_{PWM}(s)$ depicts the effect of the time delay in the digital control and Pulse Width Modulation (PWM). $G_{ci}(s)$ and $G_{vi}(s)$ are the inner P current controller and outer PR voltage controller, respectively.

$$G_{ci}(s)=K_{pi},\quad G_{vi}(s)=K_{pv}+\frac{K_{rv}s}{s^2+\omega_1^2} \tag{9}$$

where ω_1 is the system fundamental frequency.

It is worth to note that the dead time of the power switches in the real case increases the damping of the *LC*-filter [25]. This effect also affects the resonances caused by the impedance interactions of inverters. In this work, the damping effect of the dead time is modeled by increasing the series resistance in the filter inductor.

B. Current-Controlled Inverters

Fig. 5 depicts the control block diagram for the current-controlled inverters. The current in the grid-side inductor of the *LCL*-filter is controlled for a better stability, and the PR controller in the stationary $\alpha\beta$-frame is used in the current control loop. The second-order Phase-Locked Loop (PLL) is adopted for grid synchronization [26].

The PLL also affects the output impedance of the inverter besides the current control loop [21]. However, since the PLL is normally designed with a low bandwidth to filter harmonic disturbance [26], the effect of PLL dynamics on the harmonic resonance is disregarded. Thus, the current control loop itself can be modeled as a real scalar system.

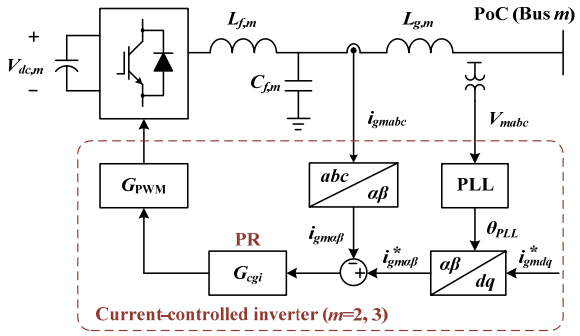

Fig. 5. Control block diagram of the current-controlled inverter.

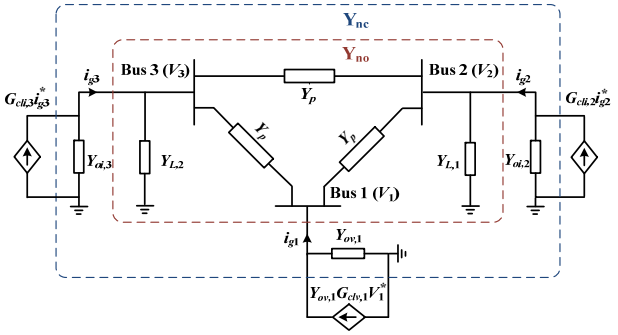

Fig. 6. Impedance-based equivalent circuit for the studied power system.

The current reference-to-output transfer function and the closed-loop output admittance can be derived as

$$G_{cli,m}(s)=\frac{T_c(s)}{1+T_c(s)},\quad Y_{oi,m}(s)=\frac{Y_o(s)}{1+T_c(s)} \tag{10}$$

where $T_c(s)$ is the open-loop gain of the current-control loop, $Y_o(s)$ is the output admittance of the *LCL*-filter, which are

$$T_c(s)=\frac{Z_{Cf,m}(s)G_{cgi}(s)G_{PWM}(s)}{Z_{Cf,m}(s)Z_{Lf,m}(s)+Z_{Lg,m}(s)Z_{Lf,m}(s)+Z_{Cf,m}(s)Z_{Lg,m}(s)} \tag{11}$$

$$Y_o(s)=\frac{Z_{Lf,m}(s)+Z_{Cf,\mathrm{m}}(s)}{Z_{Cf,m}(s)Z_{Lf,m}(s)+Z_{Lg,m}(s)Z_{Lf,m}(s)+Z_{Cf,m}(s)Z_{Lg,m}(s)} \tag{12}$$

where $Z_{Lf,m}(s)$, $Z_{Lg,m}(s)$ and $Z_{Cf,m}(s)$ are the impedances of the *LCL*-filter inductors and capacitor, respectively. $G_{cgi}(s)$ is the PR current controller, which is given by

$$G_{cgi}(s)=K_{pgi}+\frac{K_{rgi}s}{s^2+\omega_1^2} \tag{13}$$

IV. Harmonic Resonance Analysis

From Fig. 3, it is known that the system impedance seen from the PoC of each inverter is essential for the impedance-based analysis. Thus, a system impedance derivation method based on the nodal admittance matrix is developed and used in the following harmonic resonance analysis.

A. System Equivalent Circuit

Fig. 6 depicts the impedance-based equivalent circuit for the power system shown in Fig. 1. The power cables are represented as the PI-section models to include the effect of the shunt capacitors. Also, to facilitate the formulation of the nodal admittance matrix, the Thevenin model of the voltage-controlled inverter is converted to the Norton circuit.

To obtain the system impedances at the PoC of inverters, the nodal admittance matrix including the output admittances of the inverters ($\mathbf{Y_{nc}}$) is first derived as

$$\begin{bmatrix} Y_{ov,1}G_{clv,1}V_1^* \\ G_{cli,2}i_{g2}^* \\ G_{cli,3}i_{g3}^* \end{bmatrix}=\mathbf{Y_{nc}}\begin{bmatrix} V_1 \\ V_2 \\ V_3 \end{bmatrix} \tag{14}$$

$$\mathbf{Y_{nc}}=\begin{bmatrix} Y_{ov,1}+2Y_p & -Y_p & -Y_p \\ -Y_p & Y_{oi,2}+2Y_p+Y_{L,1} & -Y_p \\ -Y_p & -Y_p & Y_{oi,3}+2Y_p+Y_{L,2} \end{bmatrix} \tag{15}$$

where $Y_{ov,1}=1/Z_{ov,1}$, and Y_p is the cable admittance. Then, by inverting $\mathbf{Y_{nc}}$, the nodal impedance matrix ($\mathbf{Z_{nc}}$) is given by

$$\mathbf{Z_{nc}}=\begin{bmatrix} Z_{11} & Z_{12} & Z_{13} \\ Z_{21} & Z_{22} & Z_{23} \\ Z_{31} & Z_{32} & Z_{33} \end{bmatrix} \tag{16}$$

where the diagonal elements are the system impedances seen by the equivalent current sources of the inverters. Hence, the system impedances at the PoC of inverters can be derived by using the following relationship

$$Z_{11}=\frac{Z_{ov,1}Z_{lv,1}}{Z_{ov,1}+Z_{lv,1}},\quad Z_{22}=\frac{1}{Y_{oi,2}+Y_{li,2}},\quad Z_{33}=\frac{1}{Y_{oi,3}+Y_{li,3}} \tag{17}$$

It is noted that the $Z_{11}Y_{ov,1}$ directly depicts the close-loop response of the minor feedback loop for the voltage-controlled inverter. Similarly, the closed-loop responses for the current-controlled inverters can also be found using the nodal admittance matrix ($\mathbf{Y_{no}}$) of the connection network

$$\begin{bmatrix} i_{g1} \\ i_{g2} \\ i_{g3} \end{bmatrix}=\underbrace{\begin{bmatrix} 2Y_p & -Y_p & -Y_p \\ -Y_p & 2Y_p+Y_{L,1} & -Y_p \\ -Y_p & -Y_p & 2Y_p+Y_{L,2} \end{bmatrix}}_{\mathbf{Y_{no}}}\begin{bmatrix} V_1 \\ V_2 \\ V_3 \end{bmatrix} \tag{18}$$

Thus, the following closed-loop responses can be obtained together with (16)

$$\begin{bmatrix} i_{g,1} \\ i_{g2} \\ i_{g3} \end{bmatrix} = \mathbf{Y_{no}Z_{nc}} \begin{bmatrix} Y_{ov,1}G_{clv,1}V_1^* \\ G_{cli,2}i_{g2}^* \\ G_{cli,3}i_{g3}^* \end{bmatrix} \quad (19)$$

where the second and third diagonal elements of $\mathbf{Y_{no}}\,\mathbf{Z_{nc}}$ are corresponding to (4).

B. Impedance-Based Analysis

Table I lists the main electrical parameters of the power system, and Table II gives the voltage and current controller parameters of the inverters. The power cables adopt the same PI-section models. The current-controlled inverters are also designed with the same parameters for the sake of simplicity.

Fig. 7 depicts the frequency responses for the open-loop gains of the voltage- and current-controlled inverters, $T_v(s)$ and $T_c(s)$. It is seen that the stable terminal behavior of the inverters at the PoC are obtained with the designed controller parameters. Thus, the system resonances can be predicted by assessing the minor feedback loop gains in (5).

Fig. 8 shows the Nyquist diagrams of the minor feedback loop gains of the voltage- and current-controlled inverters. It can be seen that the minor feedback loop for the voltage-controlled inverter is unstable, whereas the minor feedback loop of the current-controlled inverters is stable. It indicates that the impedance interaction at the PoC of the voltage-controlled inverter (Bus 1) brings in harmonic resonance to the power system. In contrast, the admittance interactions at the PoC of current-controlled inverters have no contribution to trigger the harmonic resonance.

Fig. 9 shows the Nyquist diagrams of the minor feedback loop gains by reducing the proportional gains, K_{pi} and K_{pv}, of the voltage-controlled inverter (K_{pi} =5, K_{pv}=0.05) . It is seen that all the minor feedback loops in this case become stable.

TABLE I. MAIN ELECTRICAL PARAMETERS OF POWER SYSTEM

Electrical Constants		Values (p.u.[a])
Power cables (PI-section)	Series inductance (L_p)	0.005
	Seres resistance (R_p)	0.013
	Shunt capacitance (C_p)	0.01
RL load 1, 2	Resistance (R_1=R_2)	0.12
	Inductance (L_1 =L_2)	5.06
Voltage-controlled inverter 1	Filter inductor ($L_{f,1}$)	0.03
	Filter capaictor ($C_{f,1}$)	0.13
	DC-link voltage ($V_{dc,1}$)	1.88
Current-controlled inverter 2, 3	Filter inductor ($L_{f,2}$= $L_{f,3}$)	0.3
	Filter capaictor ($C_{f,2}$= $C_{f,3}$)	0.024
	Filter inductor ($L_{g,2}$= $L_{g,3}$)	0.035
	DC-link voltage ($V_{dc,2}$ =$V_{dc,3}$)	1.88
	Active power (P_2= P_3)	0.1
	Reactive power (Q_2= Q_3)	0

a. System base voltage: 400 V, base frequency: 50 Hz, and base power: 10 kVA.

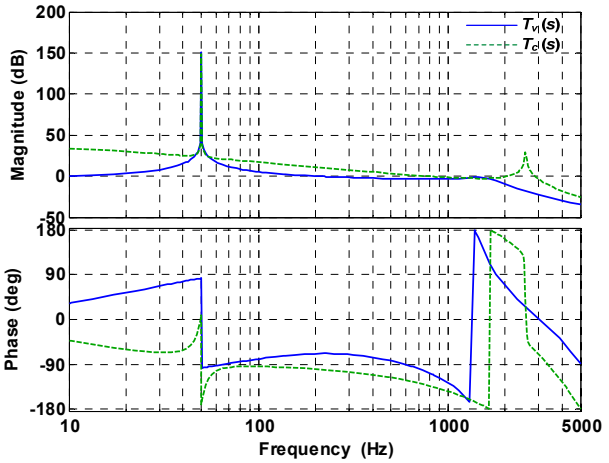

Fig. 7. Frequency responses for the open-loop gains of the voltage-controlled ($T_v(s)$) and current-controlled ($T_c(s)$) inverters.

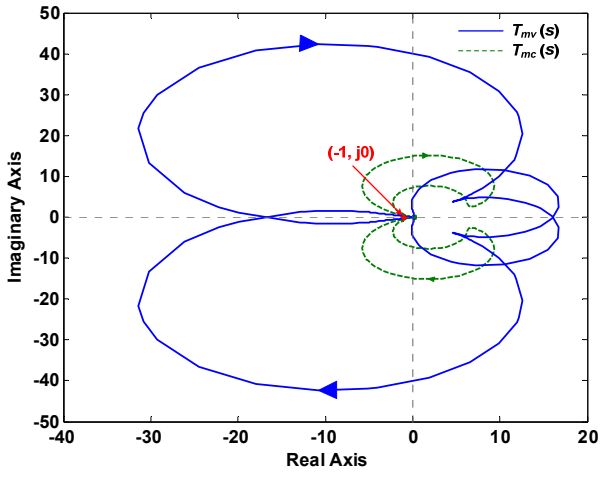

(a)

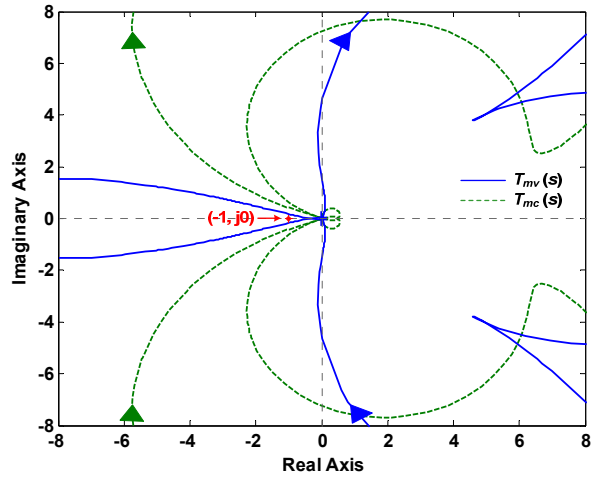

(b)

Fig. 8. Nyquist plots of the minor feedback loop gains of the inverters in the resonant case (a) Full view. (b) Zoom on (-1, j0).

TABLE II. CONTROLLER PARAMETERS OF INVERTERS

Controllers parameters			Values
Voltage-controlled inverter 1	Current controller	K_{pi}	8
	Voltage controller	K_{pv}	0.1
		K_{rv}	100
	Samping period	$T_{d,1}$	100 μs
Current-controlled inverter 2, 3	Current controller	$K_{pgi,2}$= $K_{pgi,3}$	15
		$K_{rgi,2}$= $K_{rgi,3}$	600
	Samping period	$T_{d,2}$= $T_{d,3}$	100 μs

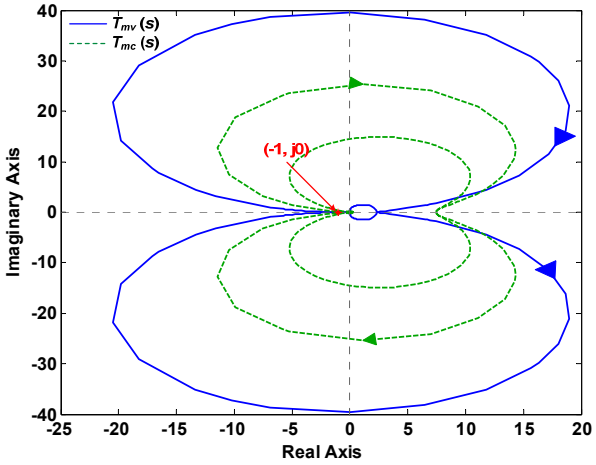

(a)

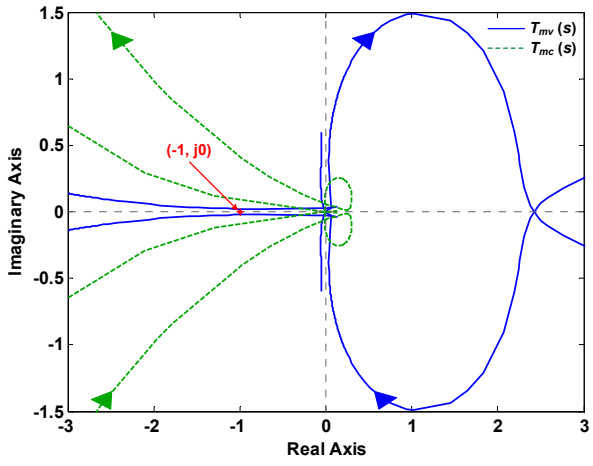

(b)

Fig. 9. Nyquist plots of the minor feedback loop gains of the inverters in the stable case (a) Full view. (b) Zoom on (-1, j0).

V. SIMULATION AND EXPERIMETNAL RESULTS

To verify the impedance-based resonance analysis, the power system shown in Fig. 1 is built in the time domain simulations by using MATLAB and PLECS Blockset, and in the laboratory test.

A. Simulation Results

Fig. 10 shows the simulated currents of the inverters with the controller parameters listed in TABLE II. The simulated bus voltages are shown in Fig. 11. It can be observed that the harmonic resonance is triggered in the power system, which confirms the frequency domain analysis in Fig. 8.

In contrast, Fig. 12 shows the simulated currents of the inverters after reducing the proportional gains in the voltage-controlled inverter (K_{pi}=5, K_{pv}=0.05). The simulated voltage at each bus of the system is shown in Fig. 13. It is obvious that the harmonic resonance in Fig. 10 and 11 are stabilized in this case, which verifies the theoretical analysis in Fig. 9. It also indicates that the harmonic resonance triggered in the system is caused by the voltage-controlled inverter other than the current-controlled inverters.

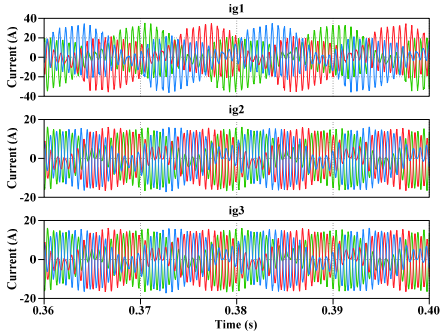

Fig. 10. Simulated output currents of the inverters in the resonant case.

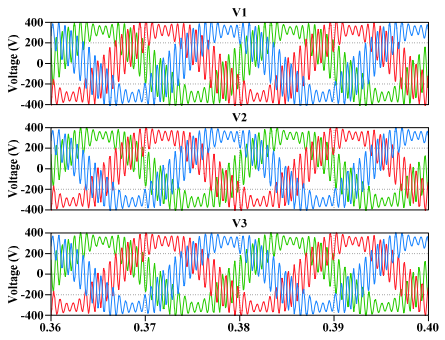

Fig. 11. Simulated bus voltages in the resonant case.

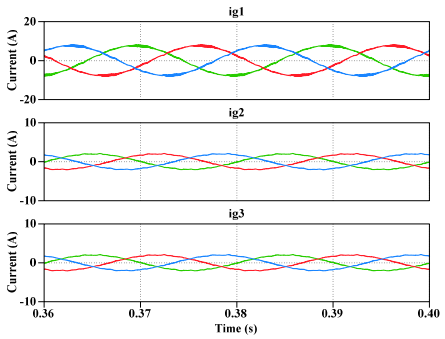

Fig. 12. Simulated output currents of the inverters in the resonant case.

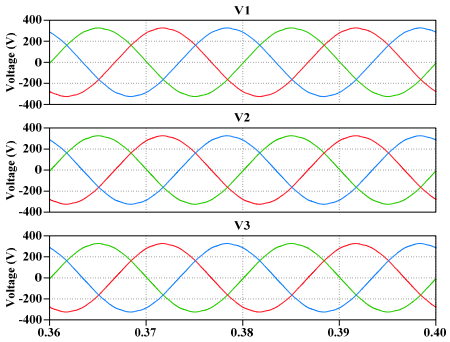

Fig. 13. Simulated bus voltages in the resonant case.

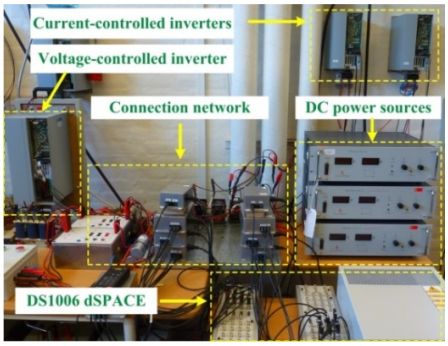

Fig. 14. Hardware picture of the built laboratory test setup.

B. Experimental Results

Fig. 14 shows a hardware picture of the built laboratory test setup. Three Danfoss frequency converters operate as a voltage-controlled and two current-controlled inverters. The control algorithm is applied in DS1006 dSPACE system.

First, the resonance case which is based on the controller parameters listed in Table II is tested. Fig. 15 shows the measured output currents of the inverters. The measured bus voltages are shown in Fig. 16. It is evident that the harmonic resonance is triggered in the power system, which matches with the simulation results shown in Fig. 10 and Fig. 11.

Then, by reducing the proportional gains in the voltage-controlled inverter (K_{pi}=5, K_{pv}=0.05), the stable case which is predicted in Fig. 9 is tested in the experiment. Fig. 17 shows the measured output currents of the inverters. The measured bus voltages are shown in Fig. 18. It is clear that the stable operation of the power system is obtained, which shows a close correlation to the theoretical analysis in Fig. 9 and the time domain simulations in Fig. 12 and Fig. 13.

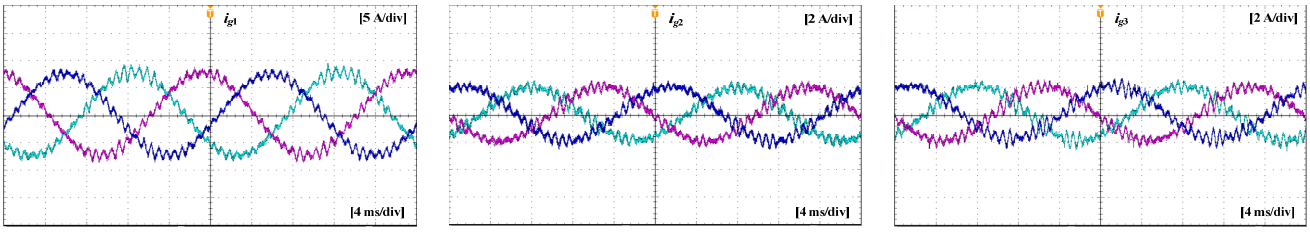

(a) (b) (c)

Fig. 15. Measured output currents of the (a) voltage-controlled inverter 1, current-controlled (b) inverter 2, and (c) inverter 3 in the resonant case.

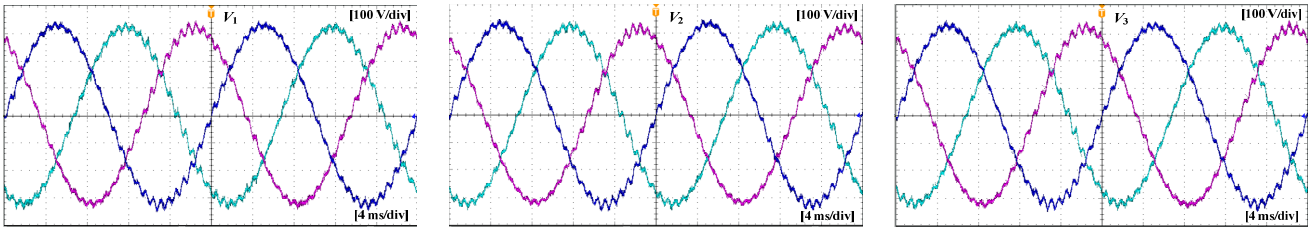

(a) (b) (c)

Fig. 16. Measured bus voltage waveforms in the resonant case. (a) Bus 1. (b) Bus 2. (c) Bus 3.

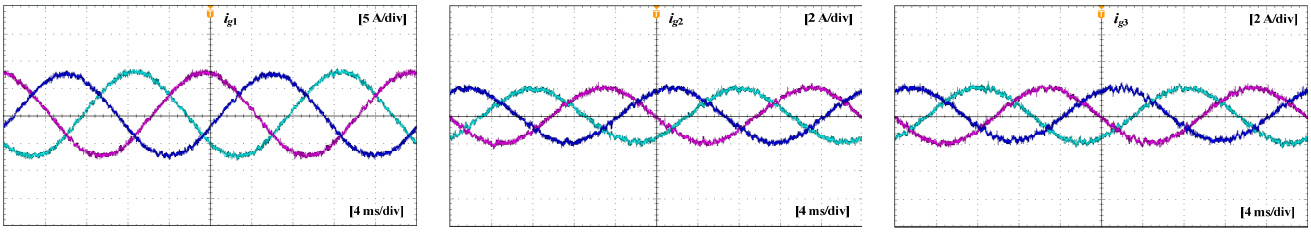

(a) (b) (c)

Fig. 17. Measured output currents of the (a) voltage-controlled inverter 1, current-controlled (b) inverter 2, and (c) inverter 3 in the stable case.

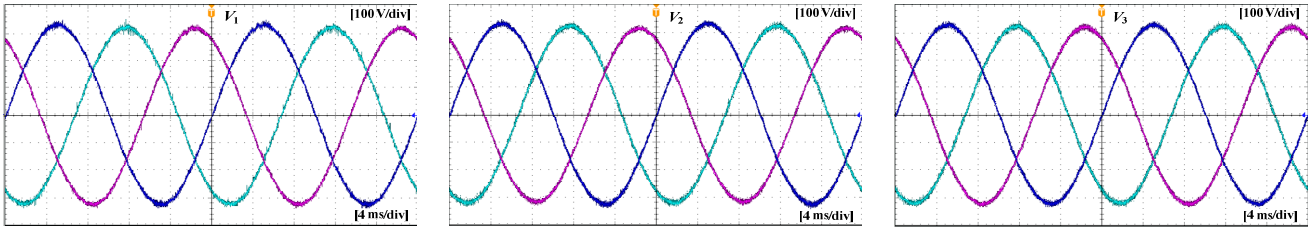

(a) (b) (c)

Fig. 18. Measured bus voltage waveforms in the stable case. (a) Bus 1. (b) Bus 2. (c) Bus 3.

VI. CONCLUSIONS

This paper has discussed a modeling and analysis method to address the harmonic resonance in the power electronics based power systems. The CCM and the impedance-based approach are briefly reviewed. It has been shown that the impedance-based approach is a more localized and design-oriented analysis tool than the CCM. Further, the impedance-based approach has been expanded to a three-phase meshed network including multiple voltage- and current- controlled inverters with *LC*- and *LCL*-filters. By the help of the nodal admittance matrix, a method for derivation of the impedance ratios has been developed. Thus, the resonance propagation caused by the impedance interactions among inverters can be easily assessed by the Nyquist stability criterion. The time domain simulations and experimental test results have been presented, which matches with the theoretical analysis.

REFERENCES

[1] F. Blaabjerg, Z. Chen, and S. B. Kjaer, "Power electronics as efficient interface in dispersed power generation systems," *IEEE Trans. Power Electron*., vol. 19, no. 5, pp. 1184-1194, Sep. 2004.

[2] P. Brogan, "The stability of multiple, high power, active front end voltage sourced converters when connected to wind farm collector system," in *Proc. EPE* 2010, pp. 1-6.

[3] J. H. Enslin and P. J. Heskes, "Harmonic interaction between a large number of distributed power inverters and the distribution network," *IEEE Trans. Power Electron.,* vol. 19, no. 6, pp. 1586-1593, Nov. 2004.

[4] J. Rocabert, A. Luna, F. Blaabjerg, and P. Rodriguez, "Control of power converters in AC microgrids," *IEEE Trans. Power Electron*., vol. 27, no. 11, pp. 4734-4749, Nov. 2012.

[5] E. Mollerstedt and B. Bernhardsson, "Out of control because of harmonics–An analysis of the harmonic response of an inverter locomotive," *IEEE Control Syst. Mag.,* vol. 20, no. 4, pp. 70-81, Aug. 2000.

[6] F. Wang, J. Duarte, M. Hendrix, and P. Ribeiro, "Modelling and analysis of grid harmonic distortion impact of aggregated DG inverters," *IEEE Trans. Power Electron.*, vol. 26, no. 3, pp. 786-797, Mar. 2011.

[7] R. Turner, S. Walton, and R. Duke, "A case study on the application of the Nyquist stability criterion as applied to interconnected loads and sources on grids," *IEEE Trans. Ind. Electron*., vol. 60, no. 7, pp. 2740-2749, Jul. 2013.

[8] J. Agorreta, M. Borrega, J. Lopez, and L. Marroyo, "Modeling and control of *N*-paralleled grid-connected inverters with *LCL* filter coupled due to grid impedance in PV plants," *IEEE Trans. Power Electron*., vol. 26, no. 3, pp. 770-785, Mar. 2011.

[9] X. Wang, F. Blaabjerg, and Z. Chen, "Autonomous control of inverter-interfaced distributed generation units for harmonic current filtering and resonance damping in an islanded microgrid," *IEEE Trans. Ind. Appl*. Early Access, 2013.

[10] N. Pogaku, M. Prodanovic, and T. Green, "Modeling, analysis and testing of autonomous operation of an inverter-based microgrid," *IEEE Trans. Power Electron*., vol. 22, no. 2, pp. 613-625, Mar. 2007.

[11] P. Kundur, *Power System Stability and Control*, McGraw-Hill Professional, 1994.

[12] G. Gaba, S. Lefebver, and D. Mukhedkar, "Comparative analysis and study of the dynamic stability of AC/DC systems," *IEEE Trans. Power Syst*., vol. 3, no. 3, pp. 978-985, Aug. 1988.

[13] Z. Yao, P. G. Therond, and B. Davat, "Stability analysis of power systems by the generalized Nyquist criterion," in *Proc. Int. Conf. CONTROL'94,* vol.1, pp. 739-744, Mar. 1994.

[14] A. MacFarlane and I. Postlethwaite, "The generalized Nyquist stability criterion and multivariable root loci," in *Int. Jour. of Control*, vol. 25, pp. 81-127, Jan. 1977.

[15] R. Middlebrook, "Input filter considerations in design and application of switching regulators," in *Proc. IEEE IAS'76*, pp. 366-382, 1976.

[16] M. Belkhayat. *Stability Criteria for AC Power Systems with Regulated Loads.* Ph.D. thesis, Purdue University, Dec. 1997.

[17] J. Sun, "Small-signal methods for AC distributed power systems–a review," *IEEE Trans. Power Electron*., vol. 24, no. 11, pp. 2545-2554, Nov., 2009.

[18] B. Wen, D. Boroyevich, P. Mattavelli, Z. Shen, and R. Burgos, "Experimental verification of the generalized Nyquist stability criterion for balanced three-phase AC systems in the presence of constant power loads," in *Proc. IEEE ECCE* 2012, pp. 3926-3933.

[19] X. Wang, F. Blaabjerg, M. Liserre, Z. Chen, J. He, and Y. Li, "An active damper for stabilizing power electronics based AC systems," in *Proc. IEEE APEC* 2013, pp. 1131-1138.

[20] M. Corradini, P. Mattavelli, M. Corradin, and F. Polo, "Analysis of parallel operation of uninterruptible power supplies loaded through long wiring cables," *IEEE Trans. Power Electron*., vol. 25, no. 4, pp. 1046-1054, Apr. 2010.

[21] L. Harnefors, M. Bongiorno, and S. Lundberg, "Input-admittance calculation and shaping for controlled voltage-source converters," *IEEE Trans. Ind. Electron*., vol. 54, no. 6, pp. 3323-3334, Dec. 2007.

[22] R. Turner, S. Walton, and R. Duke, "Stability and bandwidth implications of digitally controlled grid-connected parallel inverters," *IEEE Trans. Ind. Electron*., vol. 57, no. 11, pp. 3685-3694, Nov. 2010.

[23] S. Lefebvre, D. P. Carroll, and R. A. DeCarlo, "Decentralized power modulation of multiterminal HVDC systems," *IEEE Trans. Power Appr. Syst.*, vol. PAS-100, no. 7, pp. 3331-3339, Jul. 1981.

[24] X. Wang, F. Blaabjerg, Z. Chen, and W. Wu, "Resonance analysis in the parallel voltage-controlled DG inverters," in *Proc. IEEE APEC* 2013, pp. 2977-2983.

[25] S. Ahmed, Z. Shen, P. Mattavelli, D. Boroyevich, D. Jaksic, M. Karimi, J. Fu, "Small-signal model of a voltage source inverter (VSI) considering the dead-time effect and space vector modulation types," in *Proc. IEEE APEC* 2011, pp. 685-690.

[26] S. K. Chung, "A phase tracking system for three phase utility interface inverters," *IEEE Trans. Power Electron*., vol. 15, no. 3, pp. 431-438, May 2000.